ACS APPLIED ENERGY MATERIALS

www.acsaem.org Article

Metal Sputtering Buffer Layer for High Performance Si-Based Water Oxidation Photoanode

Chang Zhao, Beidou Guo, Guancai Xie, Chengcheng Li, Wenjing Xie, Yawen Dai, Jinlong Gong,* and Jian Ru Gong*

Cite This: *ACS Appl. Energy Mater.* 2020, 3, 8216−8223 Read Online

ABSTRACT: The sputtering deposition commonly adopted in the photoelectrochemical water splitting device usually causes structure damage and accordingly performance degradation. Taking the Si-based photoanode as a model system, we propose a facile strategy to enable sputtering deposition of the film without damaging the underlying layer by introducing a metal sputtering buffer layer, which ensures high-quality interface structure and excellent water oxidation performance. In our work, the Ni sputtering buffer layer avoids the damage on the Al_2O_3 passivation layer during the NiFe oxide electrocatalyst sputtering process. Consequently, a $Si/Al_2O_3/Ni$ metal−insulator−semiconductor junction with a precise configuration is formed, which increases the Si barrier height by reducing the interface state density and suppressing Fermi-level pinning, thus enhancing the photovoltage in thermodynamics and accelerating the oxygen evolution reaction (OER) in kinetics. In addition, the dense NiFe oxide with high transmittance and antireflection properties functions as both an efficient OER electrocatalyst and a robust protective layer and contributes to efficient use of the incident light. The photoanode affords a high water oxidation activity with an onset potential of ∼0.92 V vs reversible hydrogen electrode (V_{RHE}) and a high photocurrent density of ∼31 mA cm^{-2} at 1.23 V_{RHE} after further incorporating the cocatalyst NiFe-layered double hydroxide and has no obvious decay after 330 h of continuous operation. This strategy is beneficial for developing energy conversion devices on a large scale.

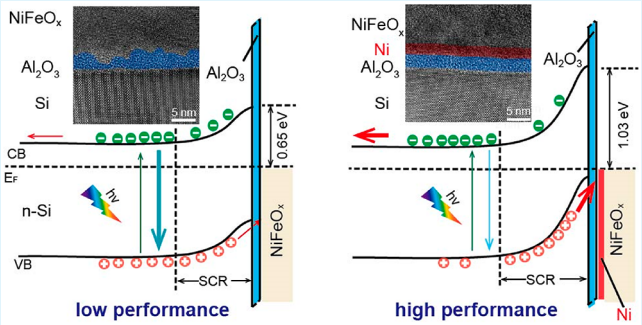

KEYWORDS: *sputtering damage, buffer layer, water oxidation, Si-based photoanode, MIS junction, photovoltage, solar water splitting, transition metal oxide*

■ INTRODUCTION

Photoelectrochemical (PEC) water splitting is one of the most promising ways to convert solar energy into renewable, sustainable, and green hydrogen energy.[1−5] In PEC devices, semiconductors usually suffer sluggish reaction kinetics and/or poor stability. To address these problems, incorporation of appropriate electrocatalysts (ECs) is indispensable. Transition metal oxides (TMOs) are widely employed as oxygen evolution reaction (OER) ECs in the PEC system due to their advanced OER catalytic activity, low cost, good light transmission, and high stability in alkaline solution. Thus, various methods such as atomic layer deposition (ALD), electrodeposition, and magnetron sputtering have been developed to deposit TMOs.[6−11] ALD, a layer-by-layer growth method for depositing materials one atomic layer at a time using surface limited reactions, is not suitable for large-scale preparation of thick TMO films due to the slow deposition rate. Electrodeposition often produces amorphous films, which cannot provide good protection for the electrode from corrosion, usually resulting in poor stability. Among these methods, magnetron sputtering with the advantages of uniform coating, fast coating, and large-scale fabrication has been widely used to deposit ECs.[12,13]

Unfortunately, it has been known that the high-energy particles bombardment during the sputtering process usually damages the underlying layer, leading to structure damage and accordingly performance degradation for photoelectronic devices such as light-emitting diodes and photovoltaic cells.[12,14] To address this issue, sputtering buffer layers including metal, alloy, metal oxide, and organic matter have been introduced into the device structure.[14−17] Increasing the thickness of the buffer layer has a better effect on decreasing damage on the underlying layer, while the possible increased light shielding might deteriorate the performance of some devices. Hence, there is a trade-off between increasing the film

Received: March 20, 2020
Accepted: August 17, 2020
Published: August 17, 2020

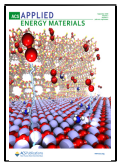

https://dx.doi.org/10.1021/acsaem.0c00609
ACS Appl. Energy Mater. 2020, 3, 8216−8223

thickness to enhance protection effect and decreasing the film thickness to achieve high optical transparency. As one type of photoelectronic device, the PEC water-splitting cell has the special complexity and uniqueness besides the common problems in other photoelectronic systems for the sputtering deposition of materials. However, as far as we know, little work has been done to explore the effect of sputtering damage and ways to tackle it in the water-splitting system.

Herein, taking the Si-based photoanode as a model system, we introduce a metal buffer layer to avoid sputtering damage on the underlying layer, which ensures a high-quality interface structure and precise device configuration and accordingly excellent PEC water oxidation performance. Specifically, a Si/Al_2O_3/Ni metal−insulator−semiconductor (MIS) junction with a strictly controlled layer thickness is formed, which contributes to increase the Si barrier height by reducing the interface state density and suppressing Fermi-level pinning,[18−29] enhancing the photovoltage in thermodynamics and accelerating the OER in kinetics. In addition, the dense sputtered $NiFeO_x$ with high transmittance functions both as a favorable EC to reduce the OER overpotential and as a protection layer against Si corrosion.[30,31] As a result, our photoanode exhibits a high activity with an onset potential of ∼0.92 V vs reversible hydrogen electrode (V_{RHE}) and a high photocurrent density of ∼31 mA cm^{-2} at 1.23 V_{RHE} after further incorporating cocatalyst NiFe-layered double hydroxide (NiFe-LDH) and has no obvious decay after 330 h of continuous operation.

■ RESULTS AND DISCUSSION

A schematic illustration of the Si/Al_2O_3/Ni/$NiFeO_x$ photoanode is shown in Figure 1. A thin film (∼2.2 nm) of Al_2O_3

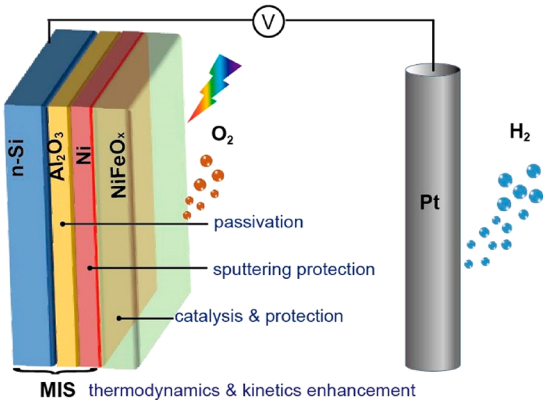

Figure 1. Schematic illustration of the PEC device with a Si/Al_2O_3/Ni/$NiFeO_x$ photoanode and a Pt counter electrode.

was first prepared on a HF-etched n-Si substrate by ALD. After that, an ultrathin Ni film (∼2 nm) was deposited on the Si/Al_2O_3 substrate by thermal evaporation. Next, a $NiFeO_x$ overlayer (∼57 nm) was coated by reactive sputtering. The thickness of each film and the content of Fe in Si/Al_2O_3/Ni/$NiFeO_x$ were optimized to yield the best PEC OER activity (Figures S1 and S2, Supporting Information). The obtained $NiFeO_x$ film is very smooth as confirmed by scanning electron microscopy (SEM) and atomic force microscopy (AFM) images (Figure S3).[32] Moreover, the photoanode with the $NiFeO_x$ film shows reduced light reflection in the entire wavelength range, demonstrating the effective antireflection property of the $NiFeO_x$ film (Figure S4a) and good transparency (Figure S4b). This broad decrease in reflectance results in an efficient incident light utilization, which is beneficial for the increase of the photocurrent density.

The structure and elemental composition of the designed photoanode were then determined by combining microscopy and spectroscopic methods. Figure 2a shows the cross-

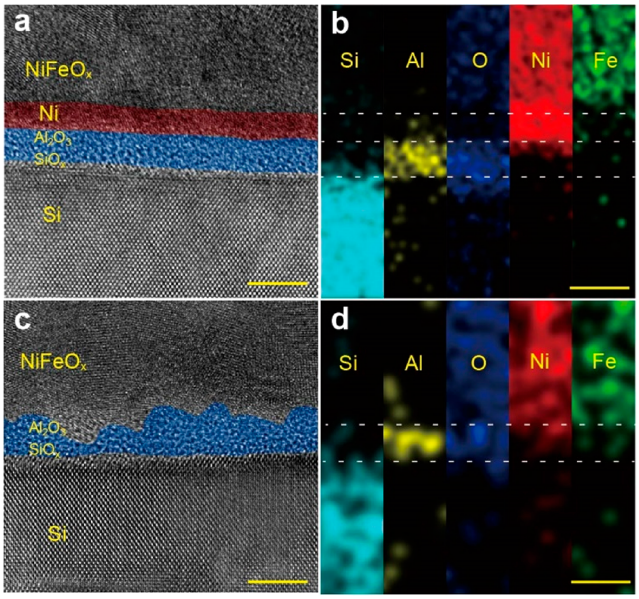

Figure 2. (a) Cs-corrected cross-sectional HRTEM image and (b) EDS mapping of the Si/Al_2O_3/Ni/$NiFeO_x$ photoanode. (c) Cs-corrected cross-sectional HRTEM image and (d) the EDS mapping of the Si/Al_2O_3/$NiFeO_x$ photoanode. Scale bars: 5 nm.

sectional spherical aberration-corrected high-resolution transmission electron micrograph (Cs-corrected HRTEM) image of the Si/Al_2O_3/Ni/$NiFeO_x$ photoanode after 30 cyclic voltammetry cycles of activation. The elemental composition of the films in the photoanode has been determined by energy-dispersive spectroscopy (EDS) mapping (Figure 2b). A thin amorphous layer (∼2.9 nm) is detected at the interface between the Si substrate and the Ni film. The thickness of the amorphous Al_2O_3 layer estimated from the EDS mapping of the Al element is ∼2.2 nm, meaning an ∼0.7 nm thick amorphous layer of SiO_x was formed by the rapid oxidation of the Si surface even after etching with HF solution. The Ni film thickness is ∼2 nm and shows obvious lattice fringes. To observe the crystal plane spacing clearly, the cross-sectional HRTEM image of the Si/Al_2O_3/Ni/$NiFeO_x$ photoanode (Figure S5a) and the zoomed-in HRTEM images of selected areas (Figure S5b−e) are analyzed. The fringe spacing of 0.18 nm is in accordance with that of the (200) lattice plane of metal Ni (Figure S5b) (PDF Card No. 04-0850). The $NiFeO_x$ overlayer shows a homogeneous distribution of Ni, Fe, and O elements, and the lattice spacing values measured in the selected area (Figure S5c−e) are in good agreement with the interplanar distances of (200), (200), and (110) lattice planes of NiO, Ni_2O_3, and Fe_2O_3, respectively.[33−36] It is seen that various thin films constituting the photoanode are uniform with clearly distinguishable boundaries. No obvious damage to the Ni film caused by the sputtering process can be identified. For comparison, we also studied the structure and elemental composition of the photoanode without the Ni film. The

https://dx.doi.org/10.1021/acsaem.0c00609
ACS Appl. Energy Mater. 2020, 3, 8216−8223

amorphous layer in this sample is nonuniform with thicknesses <1 nm in some areas (Figure 2c,d), which is due to bombardment of high-energy sputtering particles.[14,16,17] The images of the Figure 2a,c without coloring are shown in Figure S6. These results indicate that the Ni film provides an efficient buffer protection effect for the Al_2O_3 during the $NiFeO_x$ sputtering process. Hence, we conclude that the film with good crystallinity could maintain intact during the sputtering process relative to the amorphous layer and act as a sputtering buffer layer. Besides, after introduction of the Ni buffer layer, the thickness of Al_2O_3 can be precisely controlled, which plays an important role in passivating the surface states of Si. Further X-ray photoelectron spectroscopy (XPS) chemical state analysis of the $Si/Al_2O_3/Ni/NiFeO_x$ verifies that both Ni and Fe are in their oxidized forms, confirming the formation of $NiFeO_x$ (Figure S7).

The PEC OER performances of the photoanodes were evaluated by performing cyclic voltammetry in 1 M potassium hydroxide (KOH). Figure 3a shows the current dentisy−potential ($J-V$) characteristics of the designed $Si/Al_2O_3/Ni/NiFeO_x$ photoanode and the photoanode without a Ni layer. The $Si/Al_2O_3/Ni/NiFeO_x$ photoanode exhibits a low onset potential (V_{on}, which is the potential required to achieve an anodic current of 1 mA cm^{-2} in our study, Figure S8) of ∼1.00 V_{RHE}, a photocurrent density of ∼28.4 mA cm^{-2} at 1.23 V_{RHE}, and a saturated current density of ∼33.5 mA cm^{-2} (Figure 3a). In comparison, the photoanode without the Ni buffer film exhibits a higher V_{on} of ∼1.19 V_{RHE} and a much lower photocurrent density of ∼1.2 mA cm^{-2} at 1.23 V_{RHE} (Figure 3a). To ensure the reproducibility of the results, over five samples with the same configuration were tested, and the $Si/Al_2O_3/Ni/NiFeO_x$ photoanode yielded onset potentials of 1.00 ± 0.02 V_{RHE} and a photocurrent density of 28.4 ± 2 mA cm^{-2} at 1.23 V_{RHE} (Figure S9). It is clear that the OER activity of the photoanode shows significant enhancement after inserting the thin Ni sputtering buffer layer. The dark currents of these two photoanodes are negligible, indicating that the measured photocurrents under irradiation originated exclusively from photogenerated charges. The maximum applied bias photon-to-current efficiency (ABPE) of the $Si/Al_2O_3/Ni/NiFeO_x$ photoanode is calculated to be ∼1.73% at 1.12 V_{RHE} from its $J-V$ plot while assuming 100% Faradaic efficiency for the oxidation of water to O_2 (Figure S10). Stability is also an important figure of merits for Si-based photoanodes. The stability of the $Si/Al_2O_3/Ni/NiFeO_x$ was tested in 1 M KOH at a constant external bias of 1.7 V_{RHE} with a saturated photocurrent density during continuous operation. No obvious decay of the photocurrent density was observed after 330 h of continuous operation (Figure 3b). To further confirm the stability of the photoanode, we also tested the $J-V$ plot of the $Si/Al_2O_3/Ni/NiFeO_x$ photoanode after the stability test as shown in Figure S11. The photocurrent density of the $Si/Al_2O_3/Ni/NiFeO_x$ photoanode at 1.7 V_{RHE} before and after the stability test is close, which is consistent with that of the $Si/Al_2O_3/Ni/NiFeO_x$ photoanode shown in Figure 3b, indicating that the photocurrent density of the $Si/Al_2O_3/Ni/NiFeO_x$ photoanode can maintain 330 h with almost no decay. As a comparison, we also test the chronoamperometric curve of the $Si/Al_2O_3/Ni$ photoanode; the photocurrent density drops sharply in a few hundred seconds (Figure S12). These results indicate that the $NiFeO_x$ film can effectively protect Si from corrosion. The observed fluctuation in the photocurrent density could be due to the adsorption and desorption of O_2 bubbles, decrease in pH due to consumption of OH^- during continuous operation, and possible fluctuation in light intensity.[37]

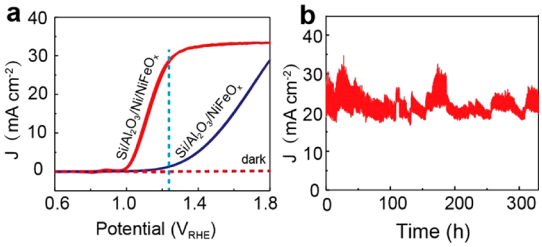

Figure 3. (a) $J-V$ curves of the photoanodes under simulated AM 1.5G solar irradiation and in the dark, in 1.0 M KOH. (b) Chronoamperometric curve of the $Si/Al_2O_3/Ni/NiFeO_x$ photoanode measured at 1.7 V_{RHE} in 1 M KOH under simulated AM 1.5G solar irradiation. The electrolyte was changed every 12 h to maintain its pH constant.

The mechanism behind the remarkable enhancement in the PEC OER performance of the $Si/Al_2O_3/Ni/NiFeO_x$ photoanode relative to that without the Ni buffer film was investigated from both thermodynamic (photovoltage, V_{ph}) and kinetic (charge separation and transfer) aspects. The V_{ph}, which is the thermodynamic driving force for the OER,[2] is the difference between the electrochemical open-circuit potential (OCP) in the dark and that under irradiation.[21,26,38] The $Si/Al_2O_3/Ni/NiFeO_x$ photoanode exhibits a V_{ph} of ∼518 mV, which shows an increase of ∼99 mV relative to the photoanode without a Ni buffer film and provides a stronger driving force for the OER (Figure 4). The V_{ph} values of the n-$Si/Al_2O_3/Ni/NiFeO_x$ and $Si/Al_2O_3/NiFeO_x$ photoanodes were also estimated by comparing the potential at 1 mA cm^{-2} of the photoanode under illumination and the nonphotoactive p^+-$Si/Al_2O_3/Ni/NiFeO_x$ and p^+-$Si/Al_2O_3/NiFeO_x$ (Figure S13),[39] which is consistent with the measured photovoltage from the OCP. After inserting the Ni film, the V_{ph} shows an increase of ∼99 mV, which can demonstrate that the passivation of surface states for the photoanode with a Ni film. Moreover, the V_{ph} is

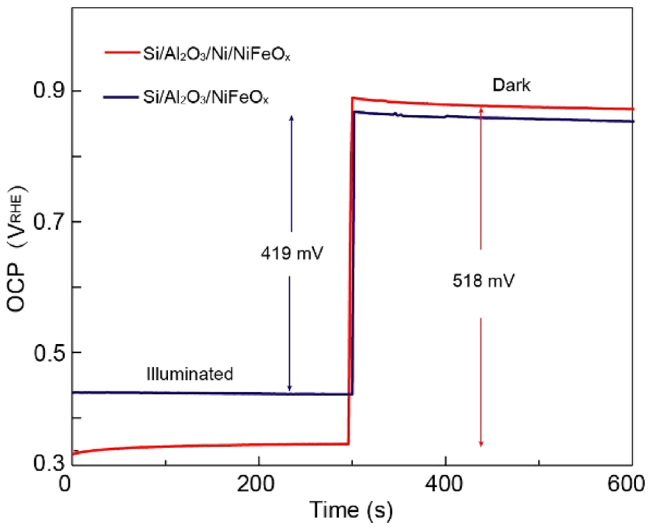

Figure 4. Electrochemical open-circuit potential measurements for the $Si/Al_2O_3/Ni/NiFeO_x$ and $Si/Al_2O_3/NiFeO_x$ photoanodes.

https://dx.doi.org/10.1021/acsaem.0c00609
ACS Appl. Energy Mater. 2020, 3, 8216−8223

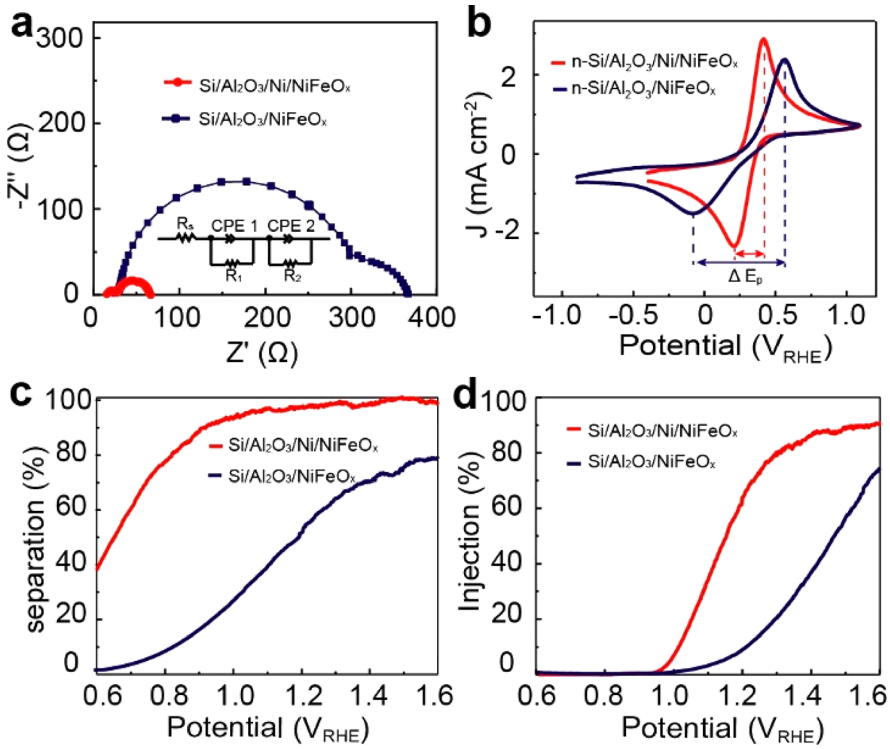

Figure 5. (a) Nyquist plots and equivalent circuit model. (b) $J-V$ curves in ferri/ferrocyanide solution. (c) Charge separation and (d) injection efficiencies of the $Si/Al_2O_3/Ni/NiFeO_x$ and $Si/Al_2O_3/NiFeO_x$ photoanodes.

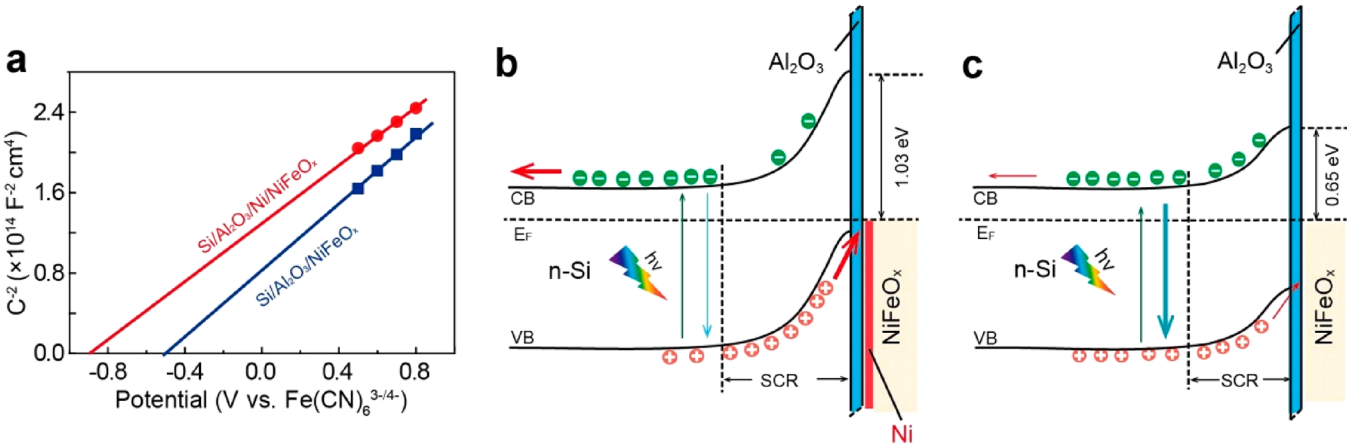

Figure 6. (a) Mott–Schottky plots and (b, c) representative energy band diagrams of the $Si/Al_2O_3/Ni/NiFeO_x$ and $Si/Al_2O_3/NiFeO_x$ photoanodes. The green, blue, and red arrows represent charge generation, recombination, and transport, while thick and thin arrows represent faster and slow rates, respectively. SCR denotes the space charge region.

one of the most important parameters influencing the V_{on}, which represents the minimum external bias required for the OER and can be described by the following equation:[37]

$$V_{on} = E^{\circ}(O_2/H_2O) + \eta_k - V_{ph} \quad (1)$$

where η_k is the overpotential and $E^{\circ}(O_2/H_2O)$ is the equilibrium potential for OER. On the basis of eq 1, η_k decreases by 91 ± 20 mV for $Si/Al_2O_3/Ni/NiFeO_x$ compared to $Si/Al_2O_3/NiFeO_x$. Taken together, both the increased V_{ph} (~99 mV) and the decreased η_k (91 ± 20 mV) contribute to a negative shift of 190 ± 20 mV in the V_{on} for $Si/Al_2O_3/Ni/NiFeO_x$. In addition, the reduced η_k shows that the OER kinetic process is accelerated in the presence of a Ni film.

We next explored the charge behaviors by tracing electrochemical impedance spectra (EIS) and fitting with an equivalent circuit model (see details in the Supporting Information). As shown in Figure 5a, the equivalent circuit model includes the system resistance (R_s), the bulk charge transfer resistance (R_1), the Si-based photoanode–electrolyte interface charge transfer resistance (R_2), and the two constant phase elements (CPE1 and CPE2), in which R_1 and R_2 correspond to the first and second semicircle of the Nyquist plots, respectively.[37,40] For the $Si/Al_2O_3/Ni/NiFeO_x$ photoanode, both R_1 and R_2 are lower than those of the $Si/Al_2O_3/NiFeO_x$ (Table S1). This result indicates that the Ni film facilitates the transport of both photogenerated charge carriers inside the bulk of the $Si/Al_2O_3/Ni/NiFeO_x$ photoanode and of

https://dx.doi.org/10.1021/acsaem.0c00609
ACS Appl. Energy Mater. 2020, 3, 8216−8223

holes across the anode−electrolyte interface. Furthermore, the conductivities of the two electrodes were compared by analyzing their $J-V$ curves in the ferri/ferrocyanide solution (Figure 5b).[41,42] The peak-to-peak separation (ΔE_p), i.e., the separation of the anodic and cathodic peaks, for the $Si/Al_2O_3/Ni/NiFeO_x$ is narrower than that of the $Si/Al_2O_3/NiFeO_x$, indicating the lower bulk resistance of the $Si/Al_2O_3/Ni/NiFeO_x$ photoanode. This suggests that inserting a Ni film in the $Si/Al_2O_3/NiFeO_x$ can effectively decrease its resistance in the bulk and improve its conductivity, which is consistent with the reduced R_1 in the EIS data.

Furthermore, we have quantitatively estimated the charge separation efficiency (η_{sep}) (Figure 5c) and injection efficiency (η_{inj}) (Figure 5d) of the photoanodes (see details in Experimental Procedures of the Supporting Information).[4,40] It is clearly seen that the $Si/Al_2O_3/Ni/NiFeO_x$ photoanode exhibits higher η_{sep} and η_{inj} than $Si/Al_2O_3/NiFeO_x$ within the entire applied bias range and achieves η_{sep} of ∼97.7% and η_{inj} of ∼70.9% at 1.23 V_{RHE}. Compared to $Si/Al_2O_3/NiFeO_x$, the inserted Ni film in $Si/Al_2O_3/Ni/NiFeO_x$ is conducive to the separation of charge and transfer of holes across the anode−electrolyte interface. Consequently, more holes in $Si/Al_2O_3/Ni/NiFeO_x$ can participate in the oxidation reaction of water relative to the photoanode without the Ni film, thereby reducing the overpotential. Therefore, the increase in both η_{sep} and η_{inj} values also demonstrates that the inserted Ni film accelerates the OER kinetics by promoting the separation of photogenerated charges and transfer of holes across the anode−electrolyte interface. The difference in light absorption between the two electrodes is negligible (Figure S14), demonstrating that the better OER activity of $Si/Al_2O_3/Ni/NiFeO_x$ is due to increased charge separation and injection rather than increasing light absorption.

We further evaluate the band structure of the photoanode before and after the introduction of the Ni film. The barrier heights of the two electrodes were calculated from Mott−Schottky plots of the photoanodes (see details in the Supporting Information).[9,43−45] The flat-band potentials (E_{fb}) of $Si/Al_2O_3/Ni/NiFeO_x$ and $Si/Al_2O_3/NiFeO_x$ are about −0.88 and −0.50 V vs $E(Fe(CN)_6^{3-/4-})$ (Figure 6a), and the barrier heights calculated from the flat-band potential for the two photoanodes are found to be 1.03 and 0.65 eV, respectively (Figure 6b,c). The Mott−Schottky plots of the $Si/Al_2O_3/Ni/NiFeO_x$ and $Si/Al_2O_3/NiFeO_x$ photoanode (Figure 6a) display that their slope is $(1.6 \pm 0.2) \times 10^{14}$. According to eq S4 in the Supporting Information, the donor concentration of the semiconductor (N_D) was calculated to be $(7.5 \pm 1) \times 10^{16}$ cm^{-3}, corresponding a resistivity of about 0.1 Ω cm for the n-Si wafer, which is in accordance with the range of 0.1−0.9 Ω cm provided by the manufacturer.[9] The sputtering of the $NiFeO_x$ film was performed under an oxygen atmosphere. It is unlikely to form a new metal Al phase from the unstable Al_2O_3 under this oxygen atmosphere to reduce the work function near the interface. We can exclude that the decrease of the barrier height for the photoanode without a Ni layer is not caused by the formation of a new metal Al phase. The Ni and Fe elements in the prepared $NiFeO_x$ film exist in their oxidation states, which have been proved by the XPS analysis (Figure S7). It is widely known that the work function of the nickel oxide is higher than that of the Ni.[21] Without consideration of the Fermi-level pinning, the $Si/Al_2O_3/NiFeO_x$ photoanode should have larger band bending relative to the $Si/Al_2O_3/Ni/NiFeO_x$ photoanode since $NiFeO_x$ possesses a larger work function than Ni. However, the opposite result that the photoanode with a Ni layer exhibits larger band bending than that of the photoanode without a Ni layer is shown, indicating that the work function difference between Ni and $NiFeO_x$ is not the main cause for the different barrier height, and thus the surface states Fermi-level pinning on the Si surface of the $Si/Al_2O_3/NiFeO_x$ photoanode cannot be ignored.

To demonstrate the presence of the surface states and Fermi-level pinning, we tested the solid-state device measurement of the $Si/Al_2O_3/Ni/NiFeO_x$ and $Si/Al_2O_3/NiFeO_x$ solid-state cell in the dark under atmosphere, where forward bias is defined as a positive pole of DC voltage applied on the $NiFeO_x$ electrode (Figure S15). The decrease in the surface states can be proved by the results obtained from the measurement of the solid-state $Si/Al_2O_3/Ni/NiFeO_x$ and $Si/Al_2O_3/NiFeO_x$ cells. As shown in Figure S15, the reverse saturation current density of $Si/Al_2O_3/Ni/NiFeO_x$ is lower than that of $Si/Al_2O_3/NiFeO_x$. Because the surface states act as recombination centers, lower surface state densities can decrease the reverse saturation current density.[27,46] The lower reverse saturation current density of $Si/Al_2O_3/Ni/NiFeO_x$ implies the decrease in the surface state densities on the Si surface. At the Si/SiO_x interface, the silicon atoms always have unsaturated dangling bonds, which will result in a high density of surface states.[47] To reduce the Fermi-level pinning, the insulated metal oxides such as Al_2O_3 and TiO_2 film are widely used as passivation layers to reduce the surface states density. As for the photoanode without a Ni buffer layer, the semiconductor/insulator interface is relatively unaffected by the sputtering directly. However, the Al_2O_3 passivation layer is highly affected during the sputtering process and suffers a serious damage, which affects its uniformity, leading to inferior surface passivation effects and Fermi-level pinning. These surface states tend to strongly pin the Fermi level at the Si surface of the $Si/Al_2O_3/NiFeO_x$ photoanode and result in a low barrier height. After introduction of the Ni buffer layer, the Al_2O_3 without damage can significantly passivate the interface states and thus alleviate the Fermi level pinning and as a result obtain a higher barrier height relative to $Si/Al_2O_3/NiFeO_x$. We therefore conclude that the obtained intact Al_2O_3 film due to the insertion of the Ni film can effectively passivate the Si surface states and reduce Fermi-level pinning and thereby increase the barrier height after Ni deposition. This greater barrier height leads to a higher photovoltage due to their linear relationship (eq S9).[20] In addition, this larger Si barrier height in the $Si/Al_2O_3/Ni/NiFeO_x$ promotes better separation of the photogenerated charges because of the increased distribution of the built-in electric field with increasing width of the space charge region (eq S12).[48,49] It is also conducive to decreasing the forward electronic dark current[50] arising from thermionic emission and tunneling.[51]

To further improve the OER performance of the photoanode, we electrodeposited NiFe-LDH on the surface of $Si/Al_2O_3/Ni/NiFeO_x$ as an OER cocatalyst due to its superior OER activity and layered open channel structure favorable for faster diffusion of water molecules and gaseous products. As depicted in Figure 7, after depositing NiFe-LDH, the $Si/Al_2O_3/Ni/NiFeO_x$/NiFe-LDH photoanode affords a photocurrent density of ∼31 mA cm^{-2} at 1.23 V_{RHE} under AM 1.5G, which is close to the highest reported value among previously reported n-Si-based photoanodes (Table S2). Among the reported n-Si based photoanodes without noble metals, our

https://dx.doi.org/10.1021/acsaem.0c00609
ACS Appl. Energy Mater. 2020, 3, 8216−8223

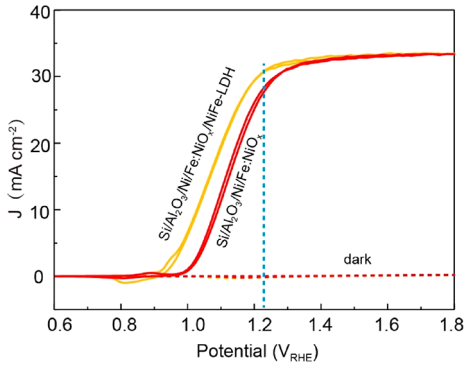

Figure 7. *J*−*V* curves of the Si/Al_2O_3/Ni/$NiFeO_x$ and Si/Al_2O_3/Ni/$NiFeO_x$/NiFe-LDH photoanodes under simulated AM 1.5G solar irradiation and in the dark, in 1.0 M KOH.

photoanode exhibits the highest photocurrent density at 1.23 V_{RHE}. Moreover, the onset potential of the photoanode with NiFe-LDH as a cocatalyst negatively shifted to ∼0.92 V_{RHE}, indicating that the water oxidation can occur at a lower external bias relative to the photoanode without NiFe-LDH. The saturated photocurrent density of the photoanode with NiFe-LDH is almost the same as that before NiFe-LDH deposition (Figure 7), which indicates that the deposited NiFe-LDH is thin enough without introducing parasitic light absorption. Besides, it is hard for us to observe this flake structure in our photoanode, further proving that the deposited NiFe-LDH is thin.

■ CONCLUSIONS

In this work, we developed a facile strategy to enable sputtering deposition of the film without damaging the underlying layer by introducing a metal sputtering buffer layer, which ensures high-quality interface structure and excellent water oxidation performance. In the Si/Al_2O_3/Ni/$NiFeO_x$ photoanode, the thin Ni film works as a sputtering buffer layer to avoid the damage from bombardment of high-energy particles on the Al_2O_3 passivation layer during the sputtering process, achieving precise control of the thickness of Al_2O_3. The thus-formed intact Si/Al_2O_3/Ni MIS junction contributes to enhancing the performance from both thermodynamics by increasing the photovoltage and kinetics by promoting charge separation in the bulk photoanode and transfer of holes across the anode−electrolyte interface. Moreover, the NiFe oxide film functions as an effective OER electrocatalyst to reduce the overpotential and a protection layer to prevent Si from corrosion, and it also shows an effective antireflection property, which contributes to efficient use of the incident light. Furthermore, we promote the OER activity of the photoanode by electrodepositing NiFe-LDH as an OER cocatalyst, resulting in a photocurrent density close to the highest value among previously reported n-Si based photoanodes. The buffer layer is important for the high quality of the photoelectrode fabricated by sputtering deposition in our experiment. Also, it should be noted that the role of the buffer layer might vary depending on the specific material, layer thickness, electrode configuration, and sputtering power. This strategy is beneficial for developing energy conversion devices on a large scale.

■ ASSOCIATED CONTENT

Supporting Information

The Supporting Information is available free of charge at https://pubs.acs.org/doi/10.1021/acsaem.0c00609.

Detailed experimental processes, select optimization data, XPS data, SEM image, AFM image, ABPE data, HRTEM image, UV−vis spectra, and the calculation process of barrier height (PDF)

■ AUTHOR INFORMATION

Corresponding Authors

Jian Ru Gong − *Chinese Academy of Sciences (CAS) Center for Excellence in Nanoscience, CAS Key Laboratory of Nanosystem and Hierarchy Fabrication, National Center for Nanoscience and Technology, Beijing 100190, P. R. China;* orcid.org/0000-0003-1512-4762; Email: gongjr@nanoctr.cn

Jinlong Gong − *Key Laboratory for Green Chemical Technology of Ministry of Education, School of Chemical Engineering and Technology, Tianjin University; Collaborative Innovation Center of Chemical Science and Engineering, Tianjin 300072, P. R. China;* orcid.org/0000-0001-7263-318X; Email: jlgong@tju.edu.cn

Authors

Chang Zhao − *Chinese Academy of Sciences (CAS) Center for Excellence in Nanoscience, CAS Key Laboratory of Nanosystem and Hierarchy Fabrication, National Center for Nanoscience and Technology, Beijing 100190, P. R. China; University of CAS, Beijing 100049, P. R. China*

Beidou Guo − *Chinese Academy of Sciences (CAS) Center for Excellence in Nanoscience, CAS Key Laboratory of Nanosystem and Hierarchy Fabrication, National Center for Nanoscience and Technology, Beijing 100190, P. R. China; University of CAS, Beijing 100049, P. R. China*

Guancai Xie − *Chinese Academy of Sciences (CAS) Center for Excellence in Nanoscience, CAS Key Laboratory of Nanosystem and Hierarchy Fabrication, National Center for Nanoscience and Technology, Beijing 100190, P. R. China; University of CAS, Beijing 100049, P. R. China*

Chengcheng Li − *Key Laboratory for Green Chemical Technology of Ministry of Education, School of Chemical Engineering and Technology, Tianjin University; Collaborative Innovation Center of Chemical Science and Engineering, Tianjin 300072, P. R. China*

Wenjing Xie − *Chinese Academy of Sciences (CAS) Center for Excellence in Nanoscience, CAS Key Laboratory of Nanosystem and Hierarchy Fabrication, National Center for Nanoscience and Technology, Beijing 100190, P. R. China*

Yawen Dai − *Chinese Academy of Sciences (CAS) Center for Excellence in Nanoscience, CAS Key Laboratory of Nanosystem and Hierarchy Fabrication, National Center for Nanoscience and Technology, Beijing 100190, P. R. China; University of CAS, Beijing 100049, P. R. China*

Complete contact information is available at: https://pubs.acs.org/10.1021/acsaem.0c00609

Author Contributions

C.Z. and B.G. contributed equally to this work.

Notes

The authors declare no competing financial interest.

https://dx.doi.org/10.1021/acsaem.0c00609
ACS Appl. Energy Mater. 2020, 3, 8216−8223

■ ACKNOWLEDGMENTS

The authors acknowledge financial support for this work from the National Natural Science Foundation of China (21422303, 21573049, and 21872043), National Basic Research plan of China (2016YFA0201600), Beijing Natural Science Foundation (2142036), Strategic Priority Research Program of CAS (XDB36030000), Youth Innovation Promotion Association, and the Special Program of "One Belt One Road" of CAS.

■ REFERENCES

(1) Fujishima, A.; Honda, K. Electrochemical Photolysis of Water at a Semiconductor Electrode. *Nature* **1972**, *238* (5358), 37−38.

(2) Walter, M. G.; Warren, E. L.; McKone, J. R.; Boettcher, S. W.; Mi, Q.; Santori, E. A.; Lewis, N. S. Solar Water Splitting Cells. *Chem. Rev.* **2010**, *110* (11), 6446−6473.

(3) Peter, L. M.; Wijayantha, K. G. U. Photoelectrochemical Water Splitting at Semiconductor Electrodes: Fundamental Problems and New Perspectives. *ChemPhysChem* **2014**, *15* (10), 1983−1995.

(4) Zhang, K.; Dong, T.; Xie, G.; Guan, L.; Guo, B.; Xiang, Q.; Dai, Y.; Tian, L.; Batool, A.; Jan, S. U.; Boddula, R.; Thebo, A. A.; Gong, J. R. Sacrificial Interlayer for Promoting Charge Transport in Hematite Photoanode. *ACS Appl. Mater. Interfaces* **2017**, *9* (49), 42723−42733.

(5) Guo, B.; Tian, L.; Xie, W.; Batool, A.; Xie, G.; Xiang, Q.; Jan, S. U.; Boddula, R.; Gong, J. R. Vertically Aligned Porous Organic Semiconductor Nanorod Array Photoanodes for Efficient Charge Utilization. *Nano Lett.* **2018**, *18* (9), 5954−5960.

(6) Mei, B.; Permyakova, A. A.; Frydendal, R.; Bae, D.; Pedersen, T.; Malacrida, P.; Hansen, O.; Stephens, I. E. L.; Vesborg, P. C. K.; Seger, B.; Chorkendorff, I. Iron-Treated NiO as a Highly Transparent p-Type Protection Layer for Efficient Si-Based Photoanodes. *J. Phys. Chem. Lett.* **2014**, *5* (20), 3456−3461.

(7) Sun, K.; McDowell, M. T.; Nielander, A. C.; Hu, S.; Shaner, M. R.; Yang, F.; Brunschwig, B. S.; Lewis, N. S. Stable Solar-Driven Water Oxidation to O_2(g) by Ni-Oxide-Coated Silicon Photoanodes. *J. Phys. Chem. Lett.* **2015**, *6* (4), 592−598.

(8) Sun, K.; Saadi, F. H.; Lichterman, M. F.; Hale, W. G.; Wang, H.-P.; Zhou, X.; Plymale, N. T.; Omelchenko, S. T.; He, J.-H.; Papadantonakis, K. M.; Brunschwig, B. S.; Lewis, N. S. Stable Solar-Driven Oxidation of Water by Semiconducting Photoanodes Protected by Transparent Catalytic Nickel Oxide Films. *Proc. Natl. Acad. Sci. U. S. A.* **2015**, *112* (12), 3612−3617.

(9) Zhou, X.; Liu, R.; Sun, K.; Friedrich, D.; McDowell, M. T.; Yang, F.; Omelchenko, S. T.; Saadi, F. H.; Nielander, A. C.; Yalamanchili, S.; Papadantonakis, K. M.; Brunschwig, B. S.; Lewis, N. S. Interface Engineering of the Photoelectrochemical Performance of Ni-Oxide-Coated n-Si Photoanodes by Atomic-Layer Deposition of Ultrathin Films of Cobalt Oxide. *Energy Environ. Sci.* **2015**, *8* (9), 2644−2649.

(10) Park, M.-J.; Jung, J.-Y.; Shin, S.-M.; Song, J.-W.; Nam, Y.-H.; Kim, D.-H.; Lee, J.-H. Photoelectrochemical Oxygen Evolution Improved by a Thin Al_2O_3 Interlayer in a NiO_x/n-Si Photoanode. *Thin Solid Films* **2016**, *599*, 54−58.

(11) He, L.; Zhou, W.; Cai, D.; Mao, S. S.; Sun, K.; Shen, S. Pulsed Laser-Deposited n-Si/NiO_x Photoanodes for Stable and Efficient Photoelectrochemical Water Splitting. *Catal. Sci. Technol.* **2017**, *7* (12), 2632−2638.

(12) Meyer, J.; Winkler, T.; Hamwi, S.; Schmale, S.; Johannes, H.-H.; Weimann, T.; Hinze, P.; Kowalsky, W.; Riedl, T. Transparent Inverted Organic Light-Emitting Diodes with a Tungsten Oxide Buffer Layer. *Adv. Mater.* **2008**, *20* (20), 3839−3843.

(13) Acosta, M.; Méndez, R. A.; Riech, I.; Rodríguez-Pérez, M.; Rodríguez-Gattorno, G. Structural, Optical and Photoelectrochemical Properties Of tungsten Oxide Thin Films Grown by Non-Reactive RF-Sputtering. *Superlattices Microstruct.* **2019**, *127*, 123−127.

(14) Meyer, J.; Hamwi, S.; Kröger, M.; Kowalsky, W.; Riedl, T.; Kahn, A. Transition Metal Oxides for Organic Electronics: Energetics, Device Physics and Applications. *Adv. Mater.* **2012**, *24* (40), 5408−5427.

(15) Bush, K. A.; Bailie, C. D.; Chen, Y.; Bowring, A. R.; Wang, W.; Ma, W.; Leijtens, T.; Moghadam, F.; McGehee, M. D. Thermal and Environmental Stability of Semi-Transparent Perovskite Solar Cells for Tandems Enabled by a Solution-Processed Nanoparticle Buffer Layer and Sputtered Ito Electrode. *Adv. Mater.* **2016**, *28* (20), 3937−43.

(16) Hung, L.-S.; Madathil, J. Radiation Damage and Transmission Enhancement in Surface-Emitting Organic Light-Emitting Diodes. *Thin Solid Films* **2002**, *410* (1−2), 101−106.

(17) Demaurex, B.; De Wolf, S.; Descoeudres, A.; Holman, Z. C.; Ballif, C. Damage at Hydrogenated Amorphous/Crystalline Silicon Interfaces by Indium Tin Oxide Overlayer Sputtering. *Appl. Phys. Lett.* **2012**, *101* (17), 171604.

(18) Chen, Y. W.; Prange, J. D.; Dühnen, S.; Park, Y.; Gunji, M.; Chidsey, C. E. D.; McIntyre, P. C. Atomic Layer-Deposited Tunnel Oxide Stabilizes Silicon Photoanodes for Water Oxidation. *Nat. Mater.* **2011**, *10* (7), 539−544.

(19) Kenney, M. J.; Gong, M.; Li, Y.; Wu, J. Z.; Feng, J.; Lanza, M.; Dai, H. High-Performance Silicon Photoanodes Passivated with Ultrathin Nickel Films for Water Oxidation. *Science* **2013**, *342* (6160), 836−840.

(20) Hill, J. C.; Landers, A. T.; Switzer, J. A. An Electrodeposited Inhomogeneous Metal-Insulator-Semiconductor Junction for Efficient Photoelectrochemical Water Oxidation. *Nat. Mater.* **2015**, *14* (11), 1150−1155.

(21) Digdaya, I. A.; Adhyaksa, G. W. P.; Trześniewski, B. J.; Garnett, E. C.; Smith, W. A. Interfacial Engineering of Metal-Insulator-Semiconductor Junctions for Efficient and Stable Photoelectrochemical Water Oxidation. *Nat. Commun.* **2017**, *8*, 15968.

(22) Cai, Q.; Hong, W.; Jian, C.; Li, J.; Liu, W. Impact of Silicon Resistivity on the Performance of Silicon Photoanode for Efficient Water Oxidation Reaction. *ACS Catal.* **2017**, *7* (5), 3277−3283.

(23) Cai, Q.; Hong, W.; Jian, C.; Li, J.; Liu, W. Insulator Layer Engineering toward Stable Si Photoanode for Efficient Water Oxidation. *ACS Catal.* **2018**, *8* (10), 9238−9244.

(24) Lee, S. A.; Lee, T. H.; Kim, C.; Lee, M. G.; Choi, M.-J.; Park, H.; Choi, S.; Oh, J.; Jang, H. W. Tailored NiO_x/Ni Cocatalysts on Silicon for Highly Efficient Water Splitting Photoanodes Via Pulsed Electrodeposition. *ACS Catal.* **2018**, *8* (8), 7261−7269.

(25) Hong, W.; Cai, Q.; Ban, R.; He, X.; Jian, C.; Li, J.; Li, J.; Liu, W. High-Performance Silicon Photoanode Enhanced by Gold Nanoparticles for Efficient Water Oxidation. *ACS Appl. Mater. Interfaces* **2018**, *10* (7), 6262−6268.

(26) Chen, J.; Xu, G.; Wang, C.; Zhu, K.; Wang, H.; Yan, S.; Yu, Z.; Zou, Z. High-Performance and Stable Silicon Photoanode Modified by Crystalline Ni@Amorphous Co Core-Shell Nanoparticles. *ChemCatChem* **2018**, *10* (21), 5025−5031.

(27) Li, S.; She, G.; Chen, C.; Zhang, S.; Mu, L.; Guo, X.; Shi, W. Enhancing the Photovoltage of Ni/n-Si Photoanode for Water Oxidation through a Rapid Thermal Process. *ACS Appl. Mater. Interfaces* **2018**, *10* (10), 8594−8598.

(28) Singh, R.; Green, M. A.; Rajkanan, K. Review of Conductor-Insulator-Semiconductor (CIS) Solar Cells. *Sol. Cells* **1981**, *3* (2), 95−148.

(29) Luo, Z.; Liu, B.; Li, H.; Chang, X.; Zhu, W.; Wang, T.; Gong, J. Multifunctional Nickel Film Protected n-Type Silicon Photoanode with High Photovoltage for Efficient and Stable Oxygen Evolution Reaction. *Small Methods* **2019**, *3*, 1900212.

(30) Trotochaud, L.; Ranney, J. K.; Williams, K. N.; Boettcher, S. W. Solution-Cast Metal Oxide Thin Film Electrocatalysts for Oxygen Evolution. *J. Am. Chem. Soc.* **2012**, *134* (41), 17253−17261.

(31) Zhang, D.; Meng, L.; Shi, J.; Wang, N.; Liu, S.; Li, C. One-Step Preparation of Optically Transparent Ni-Fe Oxide Film Electrocatalyst for Oxygen Evolution Reaction. *Electrochim. Acta* **2015**, *169*, 402−408.

(32) Sun, K.; Park, N.; Sun, Z.; Zhou, J.; Wang, J.; Pang, X.; Shen, S.; Noh, S. Y.; Jing, Y.; Jin, S.; Yu, P. K. L.; Wang, D. Nickel Oxide Functionalized Silicon for Efficient Photo-oxidation of Water Splitting. *Energy Environ. Sci.* **2012**, *5* (7), 7872−7877.

https://dx.doi.org/10.1021/acsaem.0c00609
ACS Appl. Energy Mater. 2020, 3, 8216−8223

(33) Zhang, Y.; Ji, T.; Zhang, W.; Guan, G.; Ren, Q.; Xu, K.; Huang, X.; Zou, R.; Hu, J. A Self-Powered Broadband Photodetector Based on an n-Si(111)/p-NiO Heterojunction with High Photosensitivity and Enhanced External Quantum Efficiency. *J. Mater. Chem. C* **2017**, *5* (47), 12520−12528.
(34) Liu, A.; Meng, Y.; Zhu, H.; Noh, Y.-Y.; Liu, G.; Shan, F. Electrospun p-Type Nickel Oxide Semiconducting Nanowires for Low-voltage Field-Effect Transistors. *ACS Appl. Mater. Interfaces* **2018**, *10* (31), 25841−25849.
(35) Wu, H.; Wang, L.; Wang, Y.; Guo, S.; Shen, Z. Enhanced Microwave Performance of Highly Ordered Mesoporous Carbon Coated by Ni_2O_3 Nanoparticles. *J. Alloys Compd.* **2012**, *525*, 82−86.
(36) Patra, A. K.; Kundu, S. K.; Bhaumik, A.; Kim, D. Morphology Evolution of Single-Crystalline Hematite Nanocrystals: Magnetically Recoverable Nanocatalysts for Enhanced Facet-Driven Photoredox Activity. *Nanoscale* **2016**, *8* (1), 365−377.
(37) Guo, B.; Batool, A.; Xie, G.; Boddula, R.; Tian, L.; Jan, S. U.; Gong, J. R. Facile Integration between Si and Catalyst for High-Performance Photoanodes by a Multifunctional Bridging Layer. *Nano Lett.* **2018**, *18* (2), 1516−1521.
(38) Xu, G.; Xu, Z.; Shi, Z.; Pei, L.; Yan, S.; Gu, Z.; Zou, Z. Silicon Photoanodes Partially Covered by Ni@Ni$(OH)_2$ Core-Shell Particles for Photoelectrochemical Water Oxidation. *ChemSusChem* **2017**, *10* (14), 2897−2903.
(39) Scheuermann, A. G.; Chidsey, C. E. D.; McIntyre, P. C. Understanding Photovoltage in Insulator-Protected Water Oxidation Half-Cells. *J. Electrochem. Soc.* **2016**, *163* (3), 192−200.
(40) Yu, X.; Yang, P.; Chen, S.; Zhang, M.; Shi, G. NiFe Alloy Protected Silicon Photoanode for Efficient Water Splitting. *Adv. Energy Mater.* **2017**, *7* (6), 1601805.
(41) Ji, X.; Banks, C. E.; Crossley, A.; Compton, R. G. Oxygenated Edge Plane Sites Slow the Electron Transfer of the Ferro-/Ferricyanide Redox Couple at Graphite Electrodes. *ChemPhysChem* **2006**, *7* (6), 1337−1344.
(42) Kumar, N. A.; Nolan, H.; McEvoy, N.; Rezvani, E.; Doyle, R. L.; Lyons, M. E. G.; Duesberg, G. S. Plasma-Assisted Simultaneous Reduction and Nitrogen Doping of Graphene Oxide Nanosheets. *J. Mater. Chem. A* **2013**, *1* (14), 4431−4435.
(43) Zhou, X.; Liu, R.; Sun, K.; Papadantonakis, K. M.; Brunschwig, B. S.; Lewis, N. S. 570 mV Photovoltage, Stabilized n-Si/CoO_x Heterojunction Photoanodes Fabricated Using Atomic Layer Deposition. *Energy Environ. Sci.* **2016**, *9* (3), 892−897.
(44) Hemmerling, J.; Quinn, J.; Linic, S. Quantifying Losses and Assessing the Photovoltage Limits in Metal−Insulator−Semiconductor Water Splitting Systems. *Adv. Energy Mater.* **2020**, *10* (12), 1903354.
(45) Mikolasek, M.; Frohlich, K.; Husekova, K.; Racko, J.; Rehacek, V.; Chymo, F.; Tapajna, M.; Harmatha, L. Silicon Based Mis Photoanode for Water Oxidation: A Comparison of RuO_2 and Ni Schottky Contacts. *Appl. Surf. Sci.* **2018**, *461*, 48−53.
(46) Esposito, D. V.; Levin, I.; Moffat, T. P.; Talin, A. A. H_2 Evolution at Si-Based Metal−Insulator−Semiconductor Photoelectrodes Enhanced by Inversion Channel Charge Collection and H Spillover. *Nat. Mater.* **2013**, *12* (6), 562−568.
(47) Yao, T.; Chen, R.; Li, J.; Han, J.; Qin, W.; Wang, H.; Shi, J.; Fan, F.; Li, C. Manipulating the Interfacial Energetics of n-Type Silicon Photoanode for Efficient Water Oxidation. *J. Am. Chem. Soc.* **2016**, *138* (41), 13664−13672.
(48) Li, J.; Wang, H.; Luo, M.; Tang, J.; Chen, C.; Liu, W.; Liu, F.; Sun, Y.; Han, J.; Zhang, Y. 10% Efficiency $Cu_2ZnSn(S, Se)_4$ Thin Film Solar Cells Fabricated by Magnetron Sputtering with Enlarged Depletion Region Width. *Sol. Energy Mater. Sol. Cells* **2016**, *149*, 242−249.
(49) Li, C.; Li, A.; Luo, Z.; Zhang, J.; Chang, X.; Huang, Z.; Wang, T.; Gong, J. Surviving High-Temperature Calcination: ZrO_2 -Induced Hematite Nanotubes for Photoelectrochemical Water Oxidation. *Angew. Chem., Int. Ed.* **2017**, *56* (15), 4150−4155.
(50) Laskowski, F. A. L.; Nellist, M. R.; Qiu, J.; Boettcher, S. W. Metal Oxide/(oxy)Hydroxide Overlayers as Hole Collectors and Oxygen Evolution Catalysts on Water Splitting Photoanodes. *J. Am. Chem. Soc.* **2019**, *141* (4), 1394−1405.
(51) Card, H. C.; Rhoderick, E. H. Studies of Tunnel MOS Diodes I. Interface Effects in Silicon Schottky Diodes. *J. Phys. D: Appl. Phys.* **1971**, *4* (10), 1589−1601.

https://dx.doi.org/10.1021/acsaem.0c00609
ACS Appl. Energy Mater. 2020, 3, 8216−8223